

Development of metal oxide based formaldehyde (HCHO) sensors using laser ablated nanoparticles

A Thesis submitted by

Surajit Das

In partial fulfilment of the requirements for the award of the degree of

Doctor of Philosophy



॥ त्वं ज्ञानमयो विज्ञानमयोऽसि ॥

Indian Institute of Technology Jodhpur

Electrical Engineering

July 2023

Declaration

I hereby declare that the work presented in this Thesis titled *Development of metal oxide based formaldehyde (HCHO) sensors using laser ablated nanoparticles* submitted to the Indian Institute of Technology Jodhpur in partial fulfilment of the requirements for the award of the degree of Doctor of Philosophy, is a bonafide record of the research work carried out under the supervision of Dr Mahesh Kumar, Professor, IIT Jodhpur, Rajasthan, India and Co-Supervision of Dr. Jitendra Singh, Principal Scientist, CSIR-CEERI, Pilani, Rajasthan, India. The contents of this thesis in full or in parts, have not been submitted to, and will not be submitted by me to, any other Institute or University in India or abroad for the award of any degree or diploma.



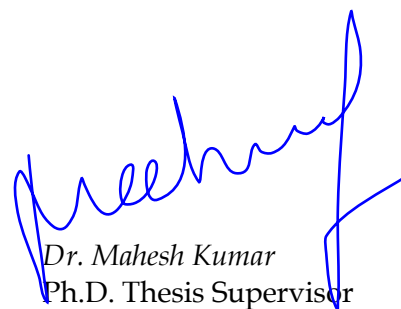
Surajit Das
P18EE202

Certificate

This is to certify that the thesis titled *Development of metal oxide based formaldehyde (HCHO) sensors using laser ablated nanoparticles*, submitted by *Surajit Das (P18EE202)* to the Indian Institute of Technology Jodhpur for the award of the degree of *Doctor of Philosophy*, is a bonafide record of the research work done by him under our supervision. To the best of our knowledge, the contents of this report, in full or in parts, have not been submitted to any other Institute or University for the award of any degree or diploma.



Dr. Jitendra Singh
Ph.D. Co-Supervisor
Principal Scientist
CSIR-CEERI, Pilani
Rajasthan, India



Dr. Mahesh Kumar
Ph.D. Thesis Supervisor
Professor
IIT Jodhpur,
Rajasthan, India

List of Figures

Figures	Title	page
1.1	Daily time spent by people in the outdoor and indoor environments.	1
1.2	Formaldehyde bond, density, molecular weight and commercial formalin source.	2
1.3	Various sources of formaldehyde in the indoor environment.	2
1.4	Various health issues due to exposure to formaldehyde in indoor areas.	2
1.5	Formalin is generally used as an embalming fluid, but nowadays, it is also used in fish to enhance their shelf-life during transportation to market.	3
1.6	Health effects due to ingestion of formalin-treated food.	3
1.7	Classification of the chemiresistive gas sensors.	4
1.8	Type of metal oxide gas sensor (a) and (b) thick film gas sensor with plastic package. (c) and (d) thin film metal oxide sensors with metal packages (TO-39 headers).	5
1.9	(a) and (c) Band diagram of metal oxide gas sensor in oxygen ambient. (b) and (d) Band diagram of metal oxide gas sensor in the presence of formaldehyde gases.	7
1.10	Type of metal oxide gas sensor and change in conductivity in the presence of reducing gases and oxidizing gas.	8
1.11	Classification of sensors according to their fabrication technology	9
1.12	Thick-film based sensor (a) optical image, (b) Schematic of sensor with package, (c) Schematic of Sensor platform and (d) Schematic of sensing layer in oxygen ambient.	10
1.13	Optical images of sputtered deposited SnO ₂ based thin film sensor.	10
1.14	Various types of nanostructured morphology used in gas sensing applications.	11
1.15	Various methods of fabrication technology for improving gas response used in metal oxide.	12
1.16	Enhancement of gas response via doping of noble metals (a) Chemical sensitization and (b) Electronic Sensitization.	12
1.17	Effect of particle sizes on gas sensing performance for metal oxide based gas sensor.	13
1.18	Effect of grain sizes on gas response .	14
1.19	Schematic illustrating the several strategies adopted for developing the formaldehyde sensor using laser ablation methods in this thesis work. First, co-planner gas sensor platform was fabricated using an Au microheater and sputtered deposited SnO ₂ thin film. Second, gas response towards HCHO was tested using laser ablated ZnO nanoparticles. Third, HCHO response has been improved via the decoration of ZnO nanoparticles on SnO ₂ thin film to form n-n heterojunction. Fourth, highly sensitive and selective p-n heterojunction based formaldehyde sensor fabricated by surface decoration of n-type SnO ₂ thin film using laser ablated p-type NiO nanoparticles.	19
2.1	Chemical benches in the clean room of CSIR-CEERI, Pilani, Rajasthan, India.	20
2.2	RF Sputtering system installed in the clean room of CSIR-CEERI, Pilani, Rajasthan, India. (a) Sputtering system, (b) Target fitted at the chamber of the system and (c) Ar plasma during sputtering.	22
2.3	(a) Pulse Laser Ablation (PLA) system installed in the clean room of CSIR-CEERI, Pilani, Rajasthan, India and (b) Schematic diagram of the Pulse Laser Ablation (PLA) system.	22
2.4	Annealing furnace (a) side view and (b) front view. (c) Oven.	23
2.5	Wire bonding machine (Hybond) at CSIR-CEERI, Pilani, Rajasthan, India: (a) machine (b) control panel and (C) bonding tool.	24
2.6	(a) Surface profiler for thickness measuring system (DektakXt, Bruker) and (b) Sheet-resistance measurement system (VEECO FPP-5000).	25
2.7	XRD system (Rigaku SmartLab, Rigaku Corporation, Tokyo, Japan) in the clean room of CSIR-CEERI, Pilani, Rajasthan, India : (a) XRD System (b) Stage and (c) Schematic diagram of XRD mechanism.	26
2.8	Atomic Force Microscopy (AFM) in the clean room of CSIR-CEERI, Pilani, Rajasthan, India.	27
2.9	FESEM characterization facility (FEI, Apreo) in the clean room of CSIR-CEERI, Pilani, Rajasthan, India.	28
2.10	Thermal imaging camera (AT-Automation Technology GmbH infra red based camera) installed at at CSIR-CEERI, Pilani, Rajasthan : (a) side view and (b) close view.	28
2.11	Probe station with Keithley-4200 SCS for electrical characterization at CSIR-CEERI,	29

	Pilani, Rajasthan, India.	
2.12	Computer controlled LabVIEW based gas sensor test set-up at CSIR-CEERI, Pilani, Rajasthan, India : (a) Glass made test chamber, (b) Schematic of connection diagram interfaced with instruments and labVIEW based measurement system and (c) Schematic of circuit diagram instruments connected with sensor and microheater.	31
3.1	(a) Layout of the gas sensor platform with microheater and interdigitated electrode (IDE), all the dimensions in micron. (b) Schematic diagram of proposed gas sensor platform. (c) Process flow diagram for the fabrication of gas sensor platform.	34
3.2	Schematic diagram of Pulse Laser Ablation (PLA) system.	34
3.3	(a) Clean alumina substrate. (b) Sputtered deposited Ti/Au thin film on alumina substrate (c) Realization of microheater and IDE pattern after laser ablation. (d) Diced chip. (e) Packaged chip on TO-39 header. (f) Wire-bonded chip for electrical characterization. (g) Packaged gas sensor platform.	35
3.4	(a) SEM images of fabricated Au microheater and IDE on alumina substrate and (b) High magnification FESEM images of microhotplate.	36
3.5	(a) TCR of gold microheater and (b) Microheater temperature variation as a function of input power.	38
3.6	(a) Microheater platform under thermal imaging camera and (b) Heat distribution profile of the Au microheater based gas sensor platform.	39
3.7	(a) Transient characteristic curve of the microhotplate at 300°C. (b) Changes in resistance of the microheater for ten successive thermal cycles at 300°C. (c) Changes in resistance of the microheater during long-term reliability test at 250°C. (d) Changes in resistance of the microheater during long-term reliability test at 350°C.	40
3.8	(a) Optical image of the Nichrome (Ni-Cr) heater based gas sensor platform. (b) SEM image of the electrode and Ni-Cr heater.	41
4.1	(a) Commercial gas sensors platform on the chuck (before deposition). (b) Gas sensors with microheater. (c) Optical image of alumina tube with Au electrode (before deposition). (d) Schematic of the sensor chip. (e) Gas sensors platform on the chuck (after deposition). (f) Gas sensor with deposited SnO ₂ thin film on Au electrode.	45
4.2	Schematic diagram of the experimental setup of a locally-assembled Pulse Laser Ablation (PLA) system.	46
4.3	XRD pattern (a) SnO ₂ thin film and (b) laser ablated ZnO nanoparticles.	47
4.4	FESEM images of the sputtered deposited SnO ₂ thin film with various thicknesses (a) having thickness of 30 nm (b) having a thickness of 40 nm (c) having a thickness of 50 nm and (d) having thickness of 60 nm.	48
4.5	FESEM images of the laser ablated ZnO nanoparticles with various ablation times (a) 30 s (b) 40 s (c) 50 s (d) 60 s (e) 50 s with high magnification and (f) 50 s with high magnification with scale .	49
4.6	(a) Sensor response of sputtered deposited SnO ₂ sensor towards formaldehyde vapor at different operating temperature from 200 – 350°C. (b) Sensor response of sputtered deposited SnO ₂ sensor towards formaldehyde vapor at different thicknesses.	50
4.7	(a) Sensor response of ZnO nanoparticles based sensor to 500 ppm formaldehyde gas at different operating temperatures in the range of 200°C – 350°C. (b) Sensor response of ZnO nanoparticles based sensor to 300 ppm formaldehyde gas at different laser ablation time at operating temperature 350°C.	50
4.8	(a) Change in resistance of the SnO ₂ sensor to formaldehyde gas concentration from 0.25 to 260 ppm at 300°C. (b) SnO ₂ sensor response to formaldehyde gas concentration from 0.25 to 260 ppm at 300°C. (c) SnO ₂ sensor response vs. formaldehyde gas concentration from 0.25 to 260 ppm at 300°C. (d) Linear fit model of SnO ₂ sensor with varying formaldehyde gas concentration from 0.25 to 260 ppm at 300°C.	52
4.9	(a) Change in resistance of the ZnO sensor to formaldehyde gas concentration from 50 to 700 ppm at 350°C. (b) ZnO sensor response to formaldehyde gas concentration from 50 to 400 ppm at 350°C. (c) SnO ₂ sensor response vs. formaldehyde concentration from 50 to 1000 ppm at 350°C. (d) Linear fit model of ZnO sensor with varying formaldehyde gas concentration from 50 to 400 ppm at 350°C.	53
4.10	(a) Response and recovery characteristics curve of the SnO ₂ sensor upon exposures	54

to 50 ppm HCHO at 300°C. (b) Response and recovery characteristics curve of the ZnO sensor upon exposures to 500 ppm HCHO at 350°C.

4.11	(a) Changes in resistance of the SnO ₂ sensor for ten successive response-recovery cycles towards 50 ppm HCHO at 300°C. (c) Changes in resistance of the ZnO sensor for ten successive response-recovery cycles towards 300 ppm HCHO at 350°C.	55
4.12	(a) Long-term reliability of the SnO ₂ sensor to 50 ppm formaldehyde at 300°C for 30 days. (b) Long-term reliability of the ZnO sensor to 500 ppm formaldehyde at 350°C for 30 days.	56
4.13	(a) Cross-response of SnO ₂ sensors towards various VOCs. (b) Cross-response of ZnO sensors towards various VOCs.	56
5.1	(a) Ni-Cr heater based gas sensor platform optical image. (b) Deposition of SnO ₂ thin film on top of alumina tube gas sensor platform (Schematic). (c) Schematic of the laser ablation process. (d) ZnO pellet in test tube arrangement. (e) Laser ablated ZnO nanoparticles enriched colloidal solution (f) Decoration of ZnO NPs using drop casting method. (g) Decorated ZnO NPs on SnO ₂ thin film (Schematic).	61
5.2	(a) Schematic of gas sensor platform in sputtering chamber. (b) Decoration of tin oxide thin film using laser ablated NiO Nanoparticles. (c) Optical images of gas sensor platform and cylindrical shape Ni pellet.	62
5.3	(a) FESEM image of pristine SnO ₂ thin film. (b) FESEM image of ZnO NPs decorated SnO ₂ sample and (c) the corresponding EDS spectra of the ZnO NPs decorated SnO ₂ sample shown in (b). (d) XRD patterns of pristine SnO ₂ and ZnO decorated SnO ₂ sample.	65
5.4	(a) FESEM image of pristine SnO ₂ thin film. (b) FESEM image of SnO ₂ thin film decorated with laser ablated NiO nanoparticles. (c) High-magnification surface image of NiO nanoparticles. (d) EDS analysis of NiO nanoparticles decorated SnO ₂ thin film.	66
5.5	(a) Change of sensor resistance in the air with a temperature of pure SnO ₂ (black) and ZnO/SnO ₂ (red). (b) Response of pristine SnO ₂ (black) and ZnO/SnO ₂ (red) to 50 ppm HCHO vapor at different operating temperatures.	67
5.6	(a) Change in sensor resistance of NiO/SnO ₂ sensor as a function of operating temperature. (b) Gas response versus operating temperature of NiO/SnO ₂ sensor to 20 ppm HCHO vapor.	67
5.7	(a) Change of resistance of ZnO/SnO ₂ sensor towards 0.25 to 200 ppm HCHO. (b) Static gas response of ZnO/SnO ₂ sensor at various gas concentrations from 0.25 to 200 ppm. (c) Response versus concentration of ZnO/SnO ₂ sensor towards different concentrations of HCHO range 0.5 to 50 ppm. (d) ZnO/ SnO ₂ sensor response fitting curves at optimal working temperature 250°C.	68
5.8	(a) Change in resistance of NiO/SnO ₂ sensor towards different concentrations of HCHO range 0.5 ppm to 50 ppm. (b) Response of NiO/SnO ₂ sensor towards different concentration of HCHO range 0.5 to 50 ppm. (c) Response versus concentration of NiO/SnO ₂ sensor towards different concentrations of HCHO range 0.5 to 50 ppm. (d) NiO/ SnO ₂ sensor response fitting curves at optimal working temperature 210°C.	70
5.9	(a) Response and recovery graph of ZnO/SnO ₂ towards 50 ppm of HCHO. (b) Response and recovery graph of NiO/SnO ₂ towards 20 ppm of HCHO.	71
5.10	(a) Short-term repeatability test of ZnO/SnO ₂ sensor towards 50 ppm of HCHO. (b) Short-term repeatability test of NiO/SnO ₂ sensor towards 20 ppm of HCHO.	72
5.11	(a) Long-term stability of ZnO/SnO ₂ sensors towards 50 ppm HCHO over the period of 30 days. (b) Long-term reliability test of the NiO/SnO ₂ sensor towards 20 ppm of HCHO for 30 days.	72
5.12	(a) Cross-response of pristine SnO ₂ and ZnO/SnO ₂ sensors towards 50 ppm concentration of HCHO and other VOCs. (b) Cross-response of SnO ₂ and NiO/SnO ₂ sensor towards 50 ppm concentration of HCHO and other VOCs.	73
5.13	(a) Change in baseline resistance due to increase of relative humidity in SnO ₂ sensor. (b) Change in baseline resistance due to increase of relative humidity in ZnO/SnO ₂ sensor.	
6.1	HCHO sensing mechanism on SnO ₂ surface. (a) Adsorbed O ₂ molecules take out electrons from SnO ₂ which leads to the generation of the EDL. (b) HCHO gas reacts with adsorbed O ⁻ ions on the SnO ₂ surface, releasing electrons that are reinjected in the conduction band and decrease in EDL.	79
6.2	Schematic diagram of the SnO ₂ sensing layer (a) in the presence of oxygen and (b) in	80

the presence of formaldehyde gases.

6.3	Schematics of HCHO gas sensing mechanism using ZnO nanoparticles.	81
6.4	(a) Proposed energy band diagram of n-type SnO ₂ and n-type ZnO heterojunctions before contact. (b) and (d) Schematic illustration of ZnO/SnO ₂ heterostructure in air after contact formation at thermal equilibrium. (c) and (e) Reduced depletion layer of ZnO/SnO ₂ heterostructure during the reaction of HCHO vapor with adsorbed O ₂ molecules after contact formation at thermal equilibrium. E _c : lower level of the conduction band, E _F : Fermi level and E _v : upper level of the valence band.	82
6.5	Schematic band diagram of pristine SnO ₂ thin film in the presence of (a) oxygen, and (b) HCHO. Schematic band diagram of NiO/SnO ₂ sensor in the presence of (c) oxygen and (d) HCHO.	83
6.6	Response behaviour of pristine SnO ₂ sensor for different concentration of HCHO (0.5, 1, 5, 10, 20, 30, 40 and 50 ppm). The fitting lines are shown in the figure by a red colour dashed line.	86
6.7	Recovery behaviour of pristine SnO ₂ sensor for different concentrations of HCHO (0.5, 1, 5, 10, 20, 30, 40 and 50 ppm). The fitting lines are shown in the figure by a red colour dashed line.	87
6.8	(a) Summarization of normalized response curves of SnO ₂ sensor towards different concentrations of HCHO range 0.5 ppm to 50 ppm at 300°C. (b) Summarization of normalized recovery curves of SnO ₂ sensor towards different concentrations of HCHO range 0.5 ppm to 50 ppm at 300°C. (c) 1/τ _{res} vs. HCHO concentration of SnO ₂ to obtain the K _a value. (d) τ _{res} vs. HCHO concentration.	88
6.9	Response behaviour of NiO/SnO ₂ sensor for different concentrations of HCHO (0.5, 1, 5, 10, 20, 30, 40 and 50 ppm). The fitting lines are shown in the figure by a red colour dashed line which was used to extract the response time of sensors towards HCHO.	90
6.10	Recovery behaviour of NiO/SnO ₂ sensor for different concentrations of HCHO (0.5, 1, 5, 10, 20, 30, 40 and 50 ppm). The fitting lines are shown in the figure by a red colour dashed line which was used to extract the recovery time of sensors towards HCHO.	91
6.11	(a) Summarization of normalized response curves of NiO/SnO ₂ sensor towards different concentrations of HCHO range 0.5 ppm to 50 ppm at 210°C. (b) Summarization of normalized recovery curves of NiO/SnO ₂ sensor towards different concentrations of HCHO range 0.5 ppm to 50 ppm at 210°C. (c) Linear fit model of NiO/SnO ₂ sensors 1/τ _{res} vs. HCHO concentration to obtain the K _a value. (d) τ _{res} vs. HCHO concentration of NiO/SnO ₂ sensor.	
7.1	(a) Freshly caught fish. (b) Cut pieces of fish sample. (c) Dipped fish sample in 10% (v/v) formalin solution. (d) Fish sample in the glass test chamber. (e) Change in resistance of sensor due to formalin-treated fish sample.	96
7.2	Scematic diagram of IoT enabled smart formaldehyde detection system for fish.	97
7.3	IoT enabled formaldehyde detection system for indoor air quality monitoring system.	97

List of Tables

<i>Table</i>	<i>Title</i>	<i>page</i>
1.1	Types of metal oxide and changes in conductivity	8
4.1	Comparative analysis of the developed sensors with previously reported sensors towards formaldehyde sensing with our fabricated SnO ₂ and ZnO sensors.	44
5.1	Comparison of various heterojunction based metal oxide sensors to HCHO gas with our fabricated ZnO/SnO ₂ sensor.	75
5.2	Comparison of various gas sensing properties of heterojunction based sensors with our fabricated NiO/SnO ₂ based sensor.	76
6.1	Summary of various parameters obtained from the fitting curve for SnO ₂	89
6.2	Summary of various parameters obtained from the fitting curve for NiO/SnO ₂	92
7.1	Comparison between various sensing material used in our present work.	95

List of Symbols

<i>Symbol</i>	<i>Description</i>
θ	Angle of incident
A	Area
E_g	Bandgap energy
Φ_B	Barrier height
k	Boltzmann constant
V_{bi}	Build-in potential
ΔI	Change in current
ΔR	Change in resistance
ΔV	Change in voltage
ΔE_c	Conduction band offset
I_a or I_o	Current in air
I_g	Current in the target gas
E_c	Conduction band energy
τ_{res}	Response time
τ_{rec}	Recovery Current
W	Depletion width
q	Electron charge
G	Electron conduction
χ	Electron affinity
μ	Electron mobility
$q\phi_r$	Energy difference in conduction band and Fermi level
ν	Frequency
η	Ideality factor
Pi	Input power
c	Lattice constant
l	Length
Φ_m	Metal work function
T	Operating temperature
h	Plank constant
n	Power coefficient
S	Relative response
R_a	Resistance in air
R_g	Resistance in the target gas
β	Response
E_v	Valance band energy
ΔE_v	Valance band offset
V_a	Voltage in air
V_g	Voltage in the target gas
λ	Wavelength
W	Watt

List of Abbreviations

<i>Abbreviation</i>	<i>Full form</i>
MOS	Metal Oxide Semiconductor
AFM	Atomic Force Microscopy
IR	Infra Red
CVD	Chemical Vapor Deposition
PVD	Physical Vapor Deposition
I-V	Current-voltage
D	Dimensional
TCR	Temperature Co-efficient of Resistance
FESEM	Field emission scanning electron microscopy
VOCs	Volatile Organic Compound
FET	Field-effect transistor
IDE	Interdigitated Electrode
IoT	Internet of Things
LED	Light-emitting diode
LDL	Low detection limit
MFC	Mass flow controller
MOCVD	Metal-organic chemical vapour deposition
Mo	Molybdenum
SnO ₂	Tin Oxide
ZnO	Zinc Oxide
NiO	Nickel Oxide
MoS ₂	Molybdenum disulfide
NR	Nanorod
NW	Nanowire
1D	One-dimensional
PL	Photoluminescence
ppm	Parts per million
ppb	Parts per billion
RF	Radiofrequency
rGO	Reduced graphene oxide
RT	Room temperature
RH	Relative humidity
SAED	Selected area electron diffraction
SEM	Scanning electron microscopy
S	Sulfur
S _v	Sulfur vacancy
SCCM	Standard cubic centimetres per minute
TE	Thermionic emission
2D	Two-dimensional
3D	Three-dimensional
TMDs	Transition metal di-chalcogenides
VOC	Volatile organic compound
VA	Vertically aligned
XRD	X-ray diffraction
0D	Zero-dimensional

